RESEARCH ARTICLE | NOVEMBER 15 2023

Dynamic interaction between phonons and edge dislocations in LiF ⊕⊘

Yang Li (10); Zexi Zheng (10); Xiang Chen (10); Youping Chen (10)



J. Appl. Phys. 134, 195104 (2023) https://doi.org/10.1063/5.0171550





CrossMark

25 November 2023 19:39:39





Cite as: J. Appl. Phys. 134, 195104 (2023); doi: 10.1063/5.0171550 Submitted: 9 August 2023 · Accepted: 21 October 2023 ·

Published Online: 15 November 2023







Yang Li, 1 D Zexi Zheng, 2 D Xiang Chen, 3 D and Youping Chen 1 D



AFFILIATIONS

- Department of Mechanical and Aerospace Engineering, University of Florida, Gainesville, Florida 32611, USA
- ²College of Mechanical Engineering, University of Shanghai for Science and Technology, Shanghai, 200093, China
- ³Department of Mechanical Engineering and Engineering Science, University of North Carolina at Charlotte, Charlotte, North Carolina 28223, USA

ABSTRACT

The dynamic interaction between phonons and dislocations in LiF has been studied using molecular dynamics simulations. The simulations have captured the strong dynamic interactions between low-frequency slow transverse acoustic phonons and dislocations that were observed in experiments. Simulation results reveal that the strong dynamic interaction is attributed to resonant interactions between dislocations and slow transverse acoustic phonons. Each dislocation segment is found to possess a set of resonant modes characterized by large-amplitude out-of-phase vibrations of atoms on both sides of the dislocation slip plane. The resonant frequencies associated with these modes exhibit a \(\mathbb{B} \) nearly linear distribution with respect to the mode order. Contrary to previous beliefs, the resonant frequencies of dislocations exhibit only a weak correlation with the dislocation length. Additionally, each dislocation exhibits a dominant resonant mode that corresponds to the strongest vibration mode in response to phonons. This dominant resonant mode is not always the first resonant mode with the lowest frestrongest vibration mode in response to phonons. This dominant resonant mode is not always the first resonant mode with the lowest frequency. Its specific order depends on the dislocation length. Simulation results have also demonstrated that the resonant modes of dislocations can be influenced by the interactions from neighboring dislocations.

Published under an exclusive license by AIP Publishing. https://doi.org/10.1063/5.0171550

I. INTRODUCTION

Over the past century, extensive research has been conducted on phonon-dislocation interaction due to its important role in thermal transport in materials. Two types of theoretical models have been developed to understand this interaction: static models focusing on the static strain field scattering and dynamic models focusing on dynamic vibrating dislocation scattering. The static models developed by Klemens¹ and those by Carruthers² address the phonon scattering by the strain field of a stationary dislocation. The models have been demonstrated to provide a reasonable agreement with experimental results for materials such as Si and Cu.^{3,4} However, when it comes to LiF^{5,6} and other materials with NaCl-type structures such as NaF, NaCl, and KCl, 7,8 the static models significantly underpredict the thermal resistance of dislocations and overpredict the thermal conductivity of materials, particularly at low temperatures where phonon-dislocation interaction dominates over phonon-phonon interaction. The disparity in thermal conductivity between theoretical and experimental results can vary by as much as five orders of magnitude. In addition, the static models fail to explain other phenomena observed in experiments on LiF, such as the polarization dependence of phonon scattering at dislocations and the substantial reduction in thermal resistance of dislocations caused by the pinning points created by γ irradiation.3

To address the qualitative and quantitative disagreements between theoretical and experimental results, subsequent studies on phonon-dislocation interaction in materials like LiF have employed theoretical models that emphasize the dynamic nature of the interaction. These dynamic models consider the scattering of phonons by a mobile dislocation, which vibrates in response to the incident phonon.^{13–20} The vibrating string model, first developed by Koehler¹⁵ and generalized by Granato and Lücke, ^{16,21} is the primary theory to quantitatively describe the dynamic phonon-dislocation interaction. This string model assumes that the vibration of a dislocation line segment (a dislocation line with two ends pinned by defects or free surfaces) under the influence of phonons is analogized to the vibration of a string under oscillating shear stress. According to the Granato-Lücke model, a dislocation segment possesses a set of resonant modes and resonant frequencies 16,21 ; for the (n + 1)th resonant

without relying on any empirical rules or parameters, except for the interatomic potential. The most commonly used methods accompanied with MD to investigate the thermal resistance of dislocations are the direct method^{25–29} and the Green–Kubo method.³⁰ Recently, to chase higher accuracy, atomistic modeling with density functional theory (DFT) and atomistic Green's function methods have been employed.^{31,32} However, these methods are computationally demanding, which limits the model size to only hundreds to thousands of atoms. In this study, we use MD simulations and the phonon wave packet (PWP) method³³ to investigate the dynamic phonon–dislocation interaction in LiF. The PWP method enables the quantification of mode-specific phonon transmissions across dislocations and provides details on the behaviors

MD is capable of studying the phonon-dislocation interaction

The rest of the article is organized as follows. In Sec. II, we introduce the methodology, including the interatomic potential and the simulation setups. In Sec. III, we present simulation results of phonon scattering at different dislocation structures, including a mobile dislocation, a pinned dislocation, dislocation segments of varying lengths, a dislocation dipole, and a pair of closely spaced dislocation segments of the same sign within the same slip plane. Simulation results regarding the mode-specific phonon transmission and dislocation behaviors at the atomic scale are also presented in this section. The paper is then ended with a brief summary and conclusions in Sec. IV.

mode (n = 0,1,2,...), the resonant frequency is proportional to (2n + 1)/L, where L is the length of the dislocation segment, and the dislocation strain caused by the mode is in the form of a sine function with a period of 2L/(2n + 1). The contribution of the mode to the phonon scattering goes down with the mode order like 1/(2n + 1). The resonant mode of dislocation is more strongly excited when the frequency of the incident phonon is closer to the corresponding resonant frequency.

The vibrating string model offers a qualitative explanation for several experimental observations in LiF. For example, it can account for the significant reduction in thermal resistance of dislocations caused by the pinning points created through γ irradiation, 3,9-12 which is a result of the alteration of dislocation lengths and subsequent modification of the resonant modes. Furthermore, the model is able to explain the experimental observations of strong polarization dependence of phonon scattering from dislocations in LiF. Specifically, only slow transverse acoustic (STA) phonons were observed to experience significant scattering by dislocations. Based on the string model, Granato and Lücke 1 and Northrop⁹ explained the phenomena as follows: the oscillation of dislocations is induced by the shear-stress component of phonons lying across the glide plane and along the Burgers vector of a dislocation, and slow transverse acoustic phonons primarily provide such shear stress. Although the vibrating string model outperforms the Klemens and Carruthers models, it still underpredicted the thermal resistance of dislocations in LiF and failed to achieve quantitative agreement with experimental observations.² To explain the discrepancy, Klemens and Carruthers suggested that a considerable number of dislocation dipoles (~30 times the dislocation density of isolated dislocations) might go undetected in the experiments.²⁰ Moreover, Klemens and Carruthers proposed speculation that dislocation dipoles possess optical vibration modes (i.e., the dislocations move in opposite directions) that can be excited by long-wavelength phonons.

The agreement with certain experimental observations suggests that the vibrating string model has effectively captured the fundamental nature of dynamic phonon-dislocation interaction. However, its limitation in considering the atomic structures of dislocations hinders its ability to accurately capture the complexity of phonon-dislocation interactions.²² In addition to the aforementioned theoretical models based on the classical elastic wave-dislocation scattering mechanism, Li et al. have proposed a quantum field theory of phonon-dislocation interaction, 23,24 in which a quantized field of dislocations, referred to as "dislon," is adopted, and a phonon interacting with a dislocation is renormalized as a quasi-phonon. The theory provides a new framework to study phonon-dislocation interaction and shows the potential to unify static and dynamic scattering mechanisms. Over the past decades, our understanding of the dynamic phonon-dislocation interaction has made limited progress, primarily due to the absence of key information and data such as specific details on dislocation motions at the atomic scale and mode-specific phonon scattering. Obtaining such information through experiments poses a significant challenge. The purpose of this study is to address this knowledge gap by providing the aforementioned information using molecular dynamics (MD) simulations and gain insights into the dynamic phonon-dislocation interaction.

II. METHODOLOGY

A. Interatomic potential

of dislocations during scattering.

A number of interatomic potentials have been developed for $\stackrel{\aleph}{\sim}$ LiF, each designed to capture specific properties or phenomena. $\vec{\phi}$ Young³⁴ developed an empirical potential for the study of ion damage in LiF crystals, while the one developed by Ishii et al.³ focuses on the thermal conductivity of molten mixtures of LiF. Among these potentials, the empirical Tosi-Fumi/Born-Mayer-Huggins potential developed by Belonoshko et al.³⁶ is the only one that has been tested for simulations of both phonons and dislocations. The phonon dispersion relations for LiF based on the potential are calculated using GULP³⁷ and presented in Fig. 1, which shows good agreement with the experimental measurements conducted by Dolling et al.³⁸ There are six phonon branches: a slow transverse acoustic (STA) phonon branch, a fast transverse acoustic (FTA) phonon branch, a longitudinal acoustic (LA) phonon branch, two transverse optical (TO1 and TO2) phonon branches, and a longitudinal optical (LO) phonon branch. This potential has been used to investigate the thermal conductivity of LiF at high temperatures (1000-4000 K) and high pressures (100-400 GPa). The obtained results agree well with the experimental measurements.³⁹ It has also been employed to study the effects of highdensity dislocations on the thermal conductivity of LiF. 40 It was demonstrated that the energies of (110) dislocation dipoles with varying spacings, obtained using the potential, were comparable to the linear elastic solution. 40 Considering these successful relevant validations, this work employs the potential developed by Belonoshko et al.³

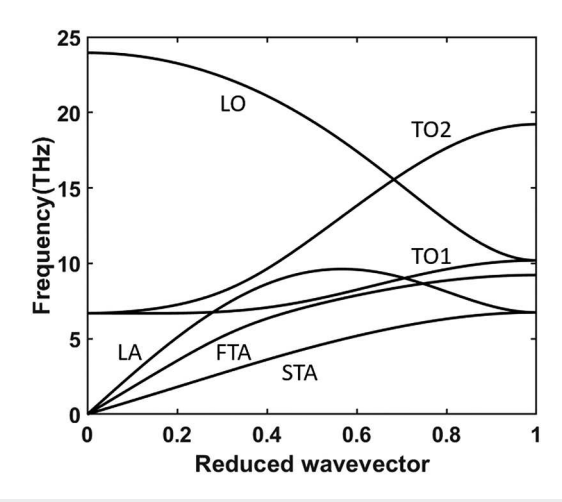


FIG. 1. The phonon dispersion relations for LiF along the [110] direction based on the empirical interatomic potential developed by Belonoshko *et al.* 36

B. Computer models

All the simulations in this work are performed using the largescale atomic/molecular massively parallel simulator (LAMMPS) software. Schematic diagrams of the MD simulation boxes are presented in Fig. 2(b). The LiF models are oriented such that the X, Y, and Z axes correspond to the $[\bar{1}10]$, [001], and [110] directions in the lattice, respectively. The dimensions of the models are 14 nm along the X direction and 1100 nm along the Z direction. The dimensions of the models along the Y direction range from 5 to 20 nm. The total number of atoms within the models varies from 10 million to 40 million. Periodic boundary conditions are applied in all three spatial directions. A dislocation structure consisting of dislocations with Burgers vectors along [110] is embedded in the central region of each model. The scattering of phonon wave packets propagating along the [110] direction at the dislocation structure is investigated using the PWP method. The orientations and dimensions of the models, as well as the dislocation structures,

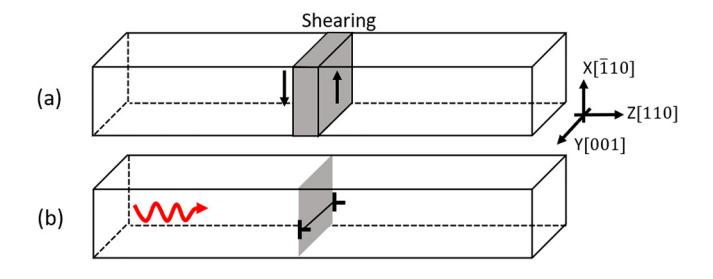


FIG. 2. (a) The orientation of the specimen in the experiments. ^{3,10} Dislocations were introduced in the wall region at the center of the specimen by shearing. (b) A schematic diagram of the MD simulation box. A dislocation structure is embedded in the center of the model. Wave packets are excited near one end of the model and allowed to propagate toward the other along the Z direction.

are constructed in accordance with the experiments by Anderson's group, 3,10 as shown in Fig. 2(a). In the experiments, 3,10 the LiF samples had a long axis aligned with the [110] direction, which was more than 10 times the length of the other two axes along the [110] and [001] directions. Dislocations with Burgers vectors along [110] were produced by shearing the wall regions at the center of the samples along the [110] direction. Thermal conductivity along the long axis of the samples was measured. Therefore, in this study, we focus on the interaction between phonons with wavevectors along the [110] direction and the dislocations with Burgers vectors along the [110] direction.

Five types of dislocation structures are investigated in this work: (1) a mobile dislocation, (2) a pinned dislocation, (3) dislocation segments of varying lengths, (4) a dislocation dipole consisting of two dislocation segments of opposite signs on closely spaced slip planes, and (5) a pair of closely spaced dislocation segments of the same sign on the same slip plane. The atomic structures of the five types of dislocations are shown in Fig. 3. A mobile dislocation is an edge dislocation in the primary (110){110} slip system of LiF. Its dislocation line and Burgers vector are oriented, respectively, along Y[001] and X[$\bar{1}10$] directions, as shown in Figs. 3(a) and 3(f). The term mobile dislocation here is used to distinguish it from a pinned dislocation and a dislocation segment, both of which are dislocations that contain vacancies. A pinned dislocation is an edge dislocation containing multiple vacancies, as shown in Figs. 3(b) and 3(g). A dislocation segment is an edge dislocation with its two ends pinned by vacancies, as shown in Figs. 3(c) and 3(h). The length of a dislocation segment is identified as the distance between the two vacancies. Since a mobile dislocation does not have any pinning points, with the periodic boundary condition along the direction of the dislocation line, its length can be considered infinite.

To embed a $1/2[\bar{1}10](110)$ edge dislocation (i.e., a mobile dislocation) into the model, two steps are taken. First, a pair of neighboring (110) planes of Li and F atoms extending from the middle to the right end of the model is removed. Next, the model is relaxed in an isobaric-isothermal ensemble for 200 ps at a temperature of 300 K and then cooled down to a temperature close to 0 K, during which the system is fully relaxed and adjusts itself to an equilibrium configuration. After relaxation, a 1/2110 edge dislocation is formed in the center of the model. A model with a pinned dislocation or a dislocation segment can be created by embedding vacancies in a model containing a 1/2110 edge dislocation. Specifically, to create a pinned dislocation, several F atoms randomly distributed along a 1/2110 edge dislocation are removed. To create a dislocation segment, two F atoms at the two ends of a $1/2[\bar{1}10](110)$ edge dislocation are removed. After relaxation, the vacancies form F-centers, which are a type of point defect in LiF, 41 and a pinned dislocation [Figs. 3(b) and 3(g)] or a dislocation segment [Figs. 3(c) and 3(h)] is formed in the center of the model. The length of the dislocation segment, L, equals the Y dimension of the model, as shown in Fig. 3(h). In this study, we investigate dislocation segments of four different lengths (5, 7, 10, and 20 nm) by constructing four models with corresponding Y dimensions. Using the same method, we build a model containing a dislocation dipole consisting of two 10 nm-long dislocation segments, and a model containing a pair of closely spaced 10 nm-long dislocation segments of the same sign within the same slip plane,

FIG. 3. Atomic structures of the five types of dislocations: (a) a mobile dislocation, (b) a pinned dislocation (a mobile dislocation + multiple vacancies), (c) a dislocation segment (a mobile dislocation + two vacancies), (d) a dislocation dipole consisting of two dislocation segments of opposite signs on closely spaced slip planes, and (e) a pair of closely spaced dislocation segments of the same sign within the same slip plane. Perspective views of the atomic structures of (f) a mobile dislocation, (g) a pinned dislocation, and (h) a dislocation segment with length L. Only the atoms near the dislocations are presented.

as shown in Figs. 3(d) and 3(e), respectively. It is noted that all the dislocation structures are obtained through MD simulations. The atomic stress component τ_{xy} near the dislocations is presented in the Appendix (see Fig. 13). As shown in Figs. 13(a)–13(c), the stress fields around an individual mobile dislocation, a pinned dislocation, and a dislocation segment are very similar, with minor differences only at the dislocation core due to point defects. However, when two dislocations are closely positioned, the stress distribution is significantly influenced, as shown in Figs. 13(d) and 13(e).

C. Phonon wave packet simulation

The phonon wave packet (PWP) method³³ is employed in the study to investigate phonon scattering at dislocations. A phonon is a quantized mode of vibration in a crystal lattice and each phonon mode is specified by a wave vector \mathbf{k} and an eigenvector \mathbf{e} . A wave packet is a linear combination of phonon modes centered at a specific wave vector. The advantage of using PWP is that it can quantitatively measure the mode dependence of the phonon–dislocation interaction and provide a visualization of the phonon scattering process, as well as the dislocation motion in response to the

influence of phonons. The phonon wave packet at position r_0 with a central wave vector \mathbf{k} can be constructed by applying the displacement field \mathbf{u} according to

$$\mathbf{u}(r) = U\mathbf{e} \exp[i\mathbf{k}(r - r_0)] \times \exp\left[-\frac{(r - r_0)^2}{\eta^2}\right],\tag{1}$$

where U is the amplitude of the wave (in this study, U = 0.001 Å), \mathbf{e} is the eigenvector, r is the position of the atom, which is coordinate Z in this work. η is the spatial extent. The eigenvector \mathbf{e} of the phonon mode with wave vector \mathbf{k} is calculated using GULP³⁷ based on the empirical potential. Only the phonon modes with wave vector \mathbf{k} along the [110] direction are investigated in this work.

The wave packets are excited near one end of the model and allowed to propagate along the Z direction toward the dislocation structures in the central region of the model, as shown in Fig. 2(b). During the process, the wave packet encounters the dislocation structure and is scattered into transmitted phonon waves and reflected phonon waves. By measuring the kinetic energy of the transmitted phonon waves (E_T) and that of the initial phonon waves (E), the energy transmission coefficient can be calculated as $\alpha=E_T/E.$

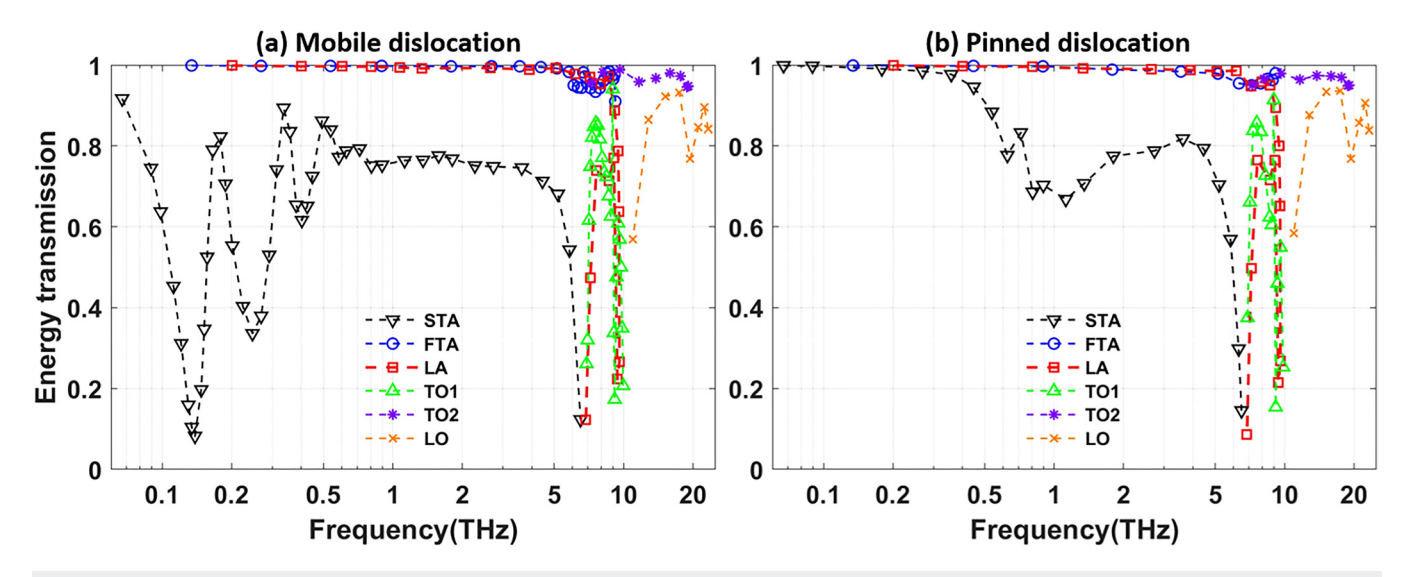


FIG. 4. The mode-specific energy transmission coefficients of phonon wave packets across (a) the mobile dislocation and (b) the pinned dislocation.

III. SIMULATION RESULTS

A. Mobile and pinned dislocations

In Fig. 4, we present the simulation results of mode-specific energy transmission coefficients of phonon wave packets across the mobile and pinned dislocations. The comparison allows us to examine the effect of the dynamic mechanism of phonon-dislocation interaction. As can be seen in Figs. 4(a) and 4(b), the energy transmission coefficients of fast transverse acoustic (FTA) phonons, longitudinal acoustic (LA) phonons, transverse optical (TO) phonons, and longitudinal optical (LO) phonons across both the mobile and pinned dislocations are close. In contrast, the energy transmission coefficients of slow transverse acoustic (STA) phonons, especially low-frequency STA phonons, across the mobile dislocation are significantly lower than those across the pinned dislocation. In addition, we studied the phonon interaction with only vacancies (with an absence of dislocations) and found the effect of vacancies to be negligible. Therefore, we conclude the significant weakening of phonon-dislocation interactions induced by vacancies is primarily attributed to their pinning effect on dislocations. It should be noted that the stress distributions around the mobile and the pinned dislocations are very similar. Consequently, the effects of the strain fields of these dislocations on phonons are also similar. Therefore, the significant difference observed in the effect of the mobile and pinned dislocations on low-frequency STA phonons primarily arises from the dynamic scattering mechanism. The results evidently demonstrate the existence of strong dynamic interactions between low-frequency STA phonons and mobile dislocations. Meanwhile, the dynamic interactions between other phonon modes and mobile dislocations are very weak. It is in good agreement with the observations by Anderson and Malinowski in their heat-pulse experiments of LiF who concluded that "A strong dynamic interaction existed for one thermal phonon mode only, the slow transverse mode."1

To acquire a quantitative understanding of the dynamic phonon-dislocation interaction on the phonon thermal transport across the dislocations, we calculate the thermal boundary resistance (TBR) of the dislocation regions in the models using the Landauer formalism and the energy transmission coefficients of 25 phonon wave packets we have measured from PWP simulations. This formalism, which was originally used to characterize the electrical resistance of a quantum conductor based on its scattering properties, 42 has been extended to quantify the TBR in terms of the energy transmission coefficients of phonons with the assumption $\overset{\varpi}{\omega}$ of equilibrium phonon distributions. Landry and McGaughey further developed it for nonequilibrium phonon distributions. 44 In this work, we adopt the expression for TBR developed by Landry and McGaughey. The phonon lifetimes in the expression are calculated using ALAMODE. 45 In both experiments 3,10 and our simulations, the long axis of the specimen is significantly longer than the other two axes. As a result, the phonons that primarily influence phonon transport across the dislocations are those propagating along the long axis or with minor angles. Therefore, we simplify the calculation by focusing on the phonons with wavevectors along the [110] direction throughout the first Brillouin zone. It is known that the number of wavevectors is determined by the model's dimension and specifically equals the number of unit cells along the normal direction. Our calculation includes every wavevector point along the [110] direction. Since the PWP simulations only provide energy transmission for a limited number of phonon modes, the energy transmission for the rest of the phonon modes is calculated through linear interpolation. 46 It should be noted that in this calculation, we focus on the difference between the thermal resistance of the dislocation regions in the models containing either mobile or pinned dislocations. Rather than determining the absolute value of thermal resistance, our aim is to gain a quantitative understanding of how the dynamic mechanism affects the

phonon-dislocation interaction and its dependence on temperature. The results are shown in Fig. 5, in which the y-axis is the ratio of the computed TBR of the region containing a mobile dislocation to that containing a pinned dislocation.

As can be seen from Fig. 5, at 1 K, the TBR of the dislocation region containing a mobile dislocation is 14 times that of the dislocation region containing a pinned dislocation. When the temperature increases to 10, 100, 300, and 600 K, this ratio decreases to 3.2, 1.6, 1.5, and 1.3. It is found that at 600 K, the ratio remains above 1, indicating that the dynamic scattering mechanism continues to have a non-negligible effect on the thermal resistance of dislocations at high temperatures. It is noted that we do not use classical MD simulations with the direct method or Green-Kubo method to measure the thermal resistance of dislocations because classical MD simulations are only suitable for studying systems at temperatures near or above the Debye temperature²⁵ (~735 K for LiF⁴⁷). This is because, in classical simulations, each normal mode shares an equal amount of energy according to the equipartition theorem, which becomes inaccurate at low temperatures due to significant quantum effects.

According to the experimental results, 3,10-12,48 at 1 K, the thermal conductivities of the LiF specimens containing pinned dislocations are twice as high as those of specimens containing unpinned dislocations. This ratio decreases from 2 to around 1 as the temperature increases to 10 K. There is a quantitative discrepancy between our simulation results and the experimental findings. Several factors may contribute to this disparity, including the higher dislocation density in our simulations (two orders of magnitude higher than observed in the experiments) and the presence of phonon-boundary scattering in the experiments, which is not considered in our simulations. It is worth noting that the measurement of dislocation density in experiments may also be prone to inaccuracies. Therefore, achieving precise quantitative agreement with experimental results is unrealistic. However, considering these factors, our simulation results show reasonable agreement with the

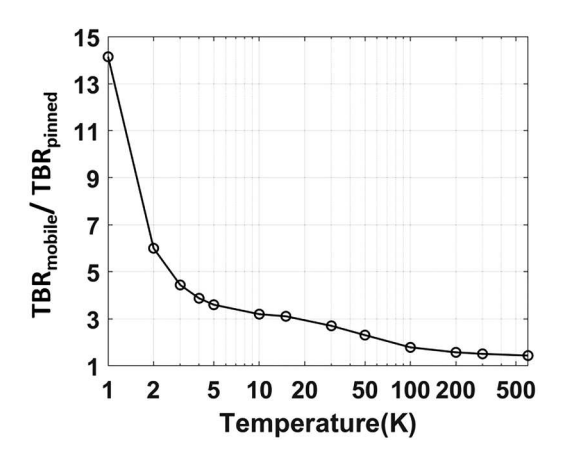


FIG. 5. The ratio of the computed thermal boundary resistance of the region containing a mobile dislocation (TBR_{mobile}) to that containing a pinned dislocation (TBRpinned) as a function of temperature.

experimental findings regarding the significant effect of mobile dislocations on the thermal conductivity of LiF at low temperatures compared to pinned dislocations.

Since it has been demonstrated that there are strong dynamic interactions exclusively between STA phonons and dislocations, we will focus on STA phonons in the following sections. To gain insight into dynamic interaction, we visualize the process of phonon scattering at dislocations through the time-sequence snapshots of the displacement response to the phonon wave packet. Figure 6 shows a series of time-sequence snapshots of STA phonon wave packets with a frequency of 0.139 THz passing across the mobile and the pinned dislocation, respectively. When the phonon wave packet encounters the mobile dislocation, large atomic displacements at the dislocation are excited, reaching up to 10.5 U, where U = 0.001 Å is the amplitude of the incident phonon wave packet. More than 90% of the energy of the phonon wave packet is reflected back by the mobile dislocation. However, when the phonon wave packet passes across the pinned dislocation, no large atomic displacements can be observed. Almost all the energy in the phonon wave packet can pass through the dislocation, indicating very weak phonon scattering at the pinned dislocation. As clearly shown in Fig. 6 (right column), the low-frequency STA phonon wave packets are negligibly affected by the stress field associated with the dislocation as they propagate across the pinned dislocation. It indicates that the reaction of low-frequency STA phonons to the stress fields of dislocations is very weak.

To visualize the dislocation motion during the scattering process with phonon wave packets, we investigate the displacements of atoms within two layers at the dislocation slip plane for both mobile and pinned dislocations. Figures 7(a) and 7(b) present manufacts of the time-sequence displacements of atoms for the snapshots of the time-sequence displacements of atoms for the mobile and pinned dislocations, respectively, under the influence of STA phonons with a frequency of 0.139 THz. The atoms near the 👼 dislocations are found to vibrate at the frequency of 0.139 THz, pri- $\overset{\omega}{\omega}$ marily along the polarization direction of STA phonons (i.e., the X direction). As can be seen from Fig. 7(a), the atoms near the mobile dislocation and on both sides of the dislocation slip plane undergo out-of-phase vibrations, with displacements of the opposite signs. The vibration amplitudes reach up to 10.5 U. In contrast, the vibration amplitudes of the atoms near the pinned dislocation are close to the amplitude of the incident phonon wave packet, as shown in Fig. 7(b). This significant difference in the motions of the dislocations results in a strong impact of the mobile dislocation on phonons and a weak impact of the pinned dislocation on phonons. The motion of the mobile dislocation under the FTA phonon with a frequency of 4.90 THz is presented in Fig. 7(c). The atoms near the mobile dislocation and on both sides of the dislocation slip plane undergo in-phase vibrations, with displacements of the same sign, along the polarization direction of FTA phonons (i.e., the Y direction). The FTA phonon mode induces strong vibrations of the mobile dislocation, reaching an amplitude of 4.9 U. However, despite the strong vibrations, the phonon scattering remains weak. The energy transmission coefficient of the FTA phonon mode remains high, reaching 94.5%. This indicates that a strong dynamic interaction between phonons and dislocations requires two essential features: strong vibrations of atoms near the dislocations and out-of-phase vibrations of atoms on both sides of the dislocation

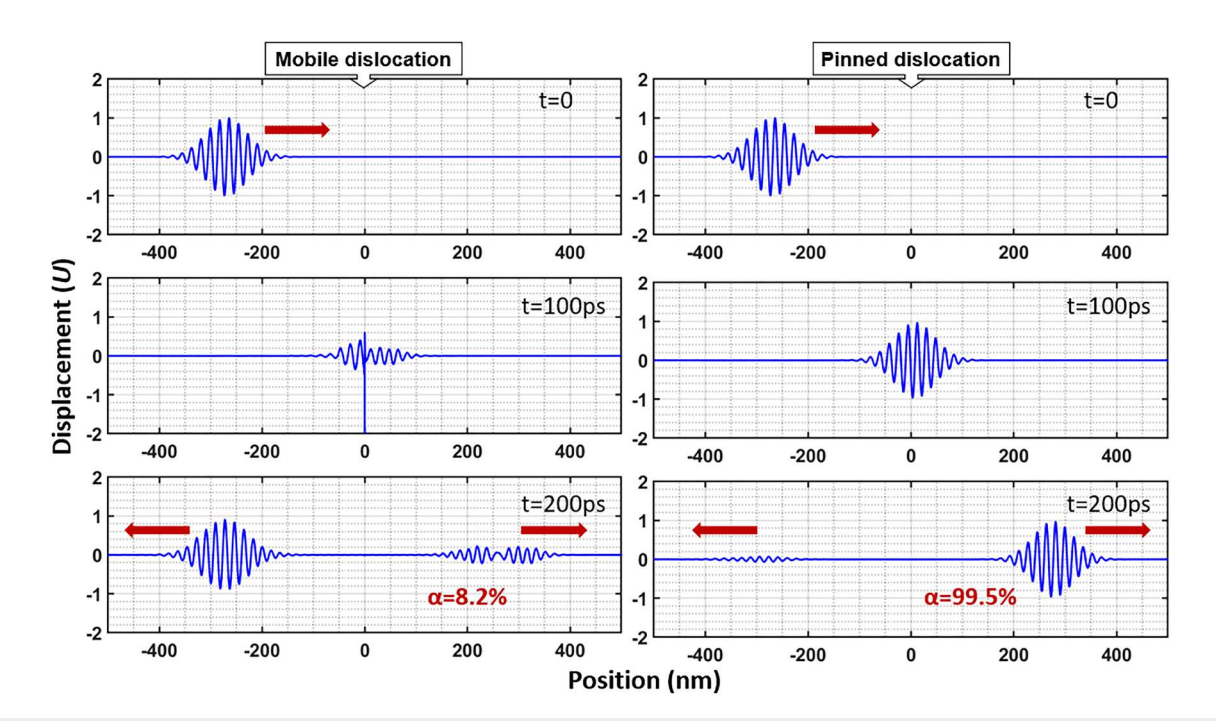


FIG. 6. Time-sequence snapshots of the displacements for STA wave packets with a frequency of 0.139 THz passing across the mobile (left column) and the pinned dislocation (right column), respectively. The unit of the displacement, *U*, denotes the amplitude of the incident phonon wave packets, which is 0.001 Å. The displacement is located at position Z = 0. The displacement of the phonon wave packet at the mobile dislocation reaches up to 10.5 *U*, exceeding the displacement range of 2 *U* depicted in the figure.

slip plane. The simulation results have confirmed and characterized the vibrations of dislocations predicted by the string model as out-of-phase vibrations of atoms on both sides of the dislocation slip plane.

In our simulations, the dislocation lies in the [110] slip plane and has the Burgers vector along $[\bar{1}10]$. It is consistent with the experimental observations that edge dislocations in LiF lie in the {110} slip planes and possess Burgers vectors along the (110) directions, as the $\langle 110 \rangle \{110\}$ slip systems are the primary slip systems in LiF. The STA phonons have polarization vectors along [110], parallel to the Burgers vector of the dislocation, while the FTA phonons have polarization vectors along [001], perpendicular to the Burgers vector of the dislocation. The simulation results show that the dislocation undergoes out-of-phase vibrations only under STA phonons, indicating the necessity of providing shear stress along the Burgers vector of dislocation for exciting out-of-phase vibrations. It confirms the prediction of the string model that only the shear-stress component of phonons along the Burgers vector of dislocation can induce the dynamic vibration of the dislocation.

In Fig. 8(a), we present the maximum vibration amplitudes of the atoms near the mobile dislocation along the three spatial directions under STA phonons with varying frequencies. The energy transmission coefficients of the STA phonons are also presented in Fig. 8(a). The results of FTA and LA phonons are presented in Figs. 8(b) and 8(c) for comparison. It is noted that in the frequency

range of 6.7 to 9.6 THz, there are two LA phonon modes at a single frequency, as shown in Fig. 1. As a result, Fig. 8(c) displays two curves of LA phonon energy transmission coefficients within the frequency range of 6.7 THz to 9.6 THz. It is found that the displacements of atoms near dislocations primarily occur along the polarization vectors of the incident phonons: STA (X direction), FTA (Y direction), and LA (Z direction). It is also found that under STA phonons, the displacements of atoms in the Z direction are also excited. Under LA phonons, the displacements of atoms in the X direction are also excited. This indicates a mode conversion between STA and LA phonons during the dynamic interaction between phonons and mobile dislocations. In contrast, under FTA phonons, the displacements of atoms occur exclusively along the Y direction, indicating the absence of mode conversion to STA or LA phonons.

The energy transmission coefficients of STA phonons across the mobile dislocation exhibit multiple transmission minima at specific frequencies, such as 0.139, 0.246, and 0.403 THz. Correspondingly, at these frequencies, the mobile dislocation displays vibration amplitude maxima, as shown in Fig. 8(a). This observation suggests that the dynamic interactions between STA phonons and dislocations are primarily the result of the excitation of the resonant vibrational modes of dislocations by STA phonons with specific frequencies. It demonstrates the prediction of the vibrating string model regarding the resonant modes of dislocations.

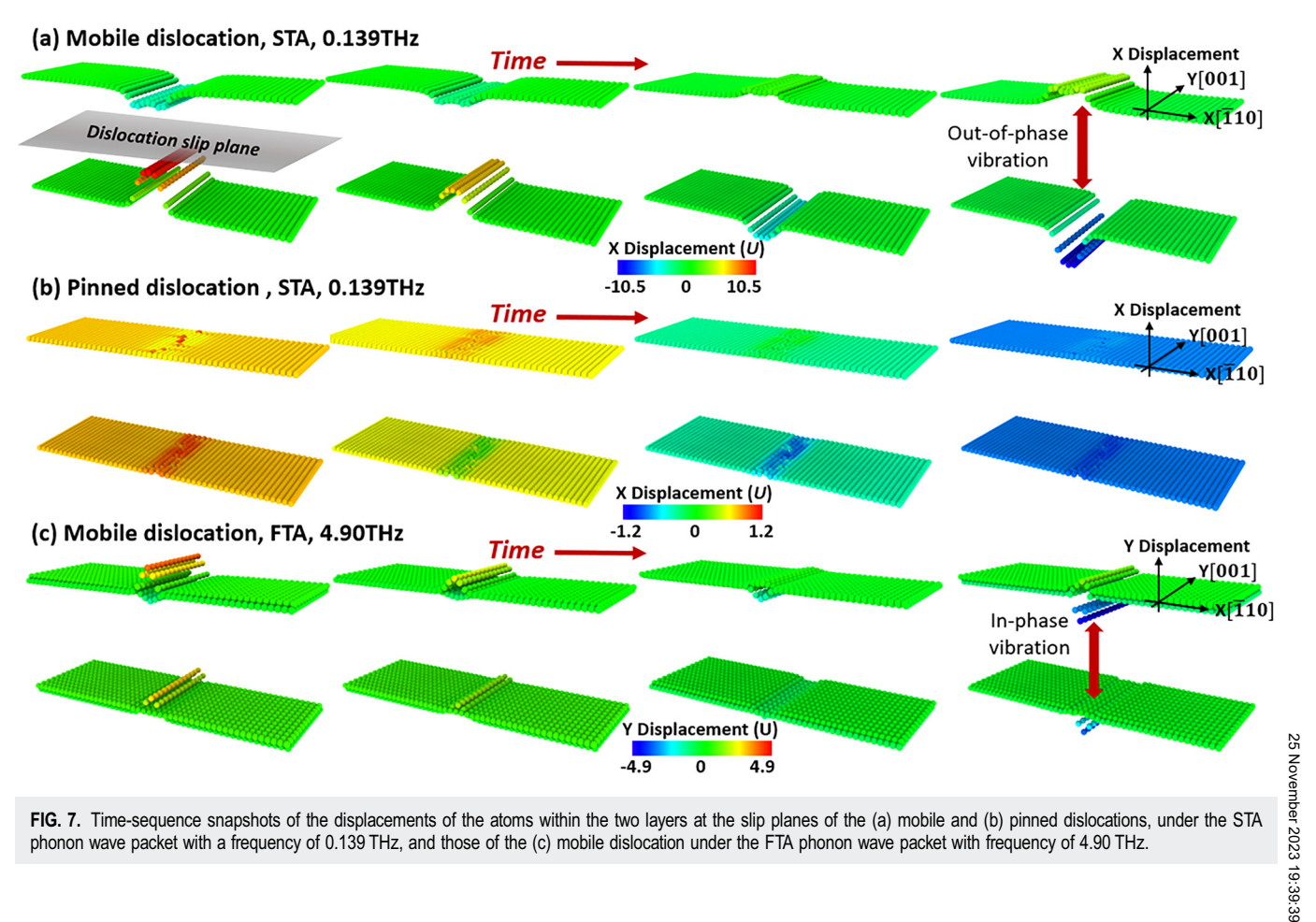


FIG. 7. Time-sequence snapshots of the displacements of the atoms within the two layers at the slip planes of the (a) mobile and (b) pinned dislocations, under the STA phonon wave packet with a frequency of 0.139 THz, and those of the (c) mobile dislocation under the FTA phonon wave packet with frequency of 4.90 THz.

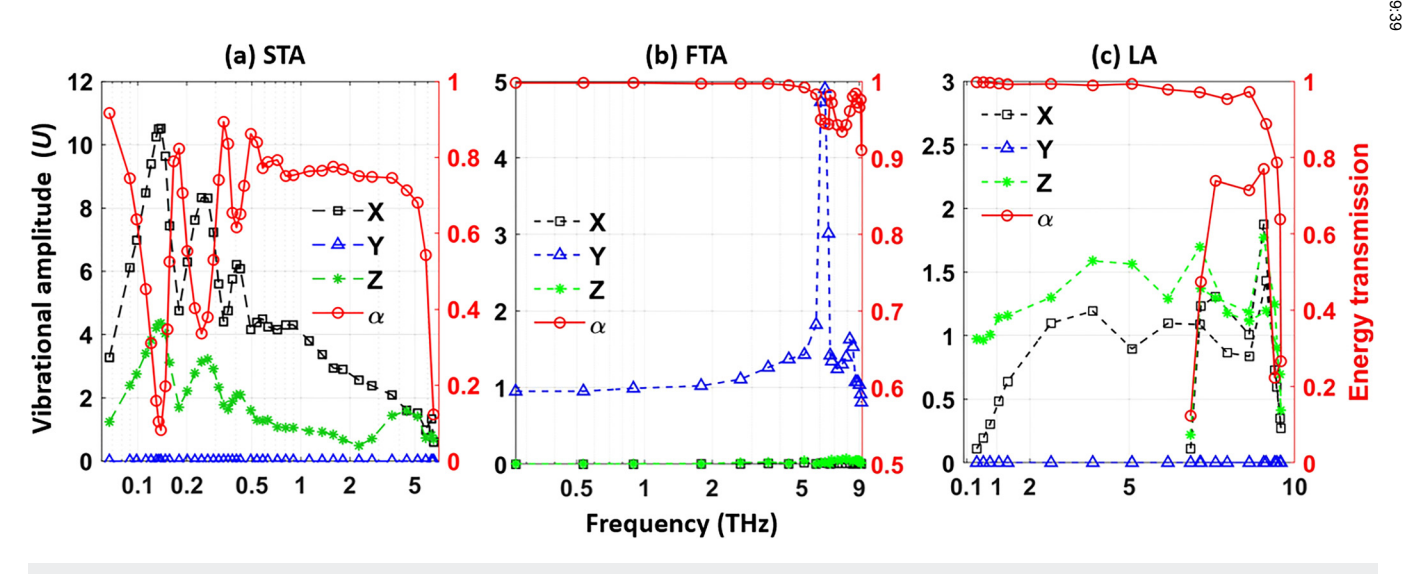


FIG. 8. The maximum vibrational amplitude of the atoms near the mobile dislocation under the (a) STA, (b) FTA, and (c) LA phonon wave packets with varying frequencies. The unit U denotes the amplitude of the phonon wave packet, which is equal to 0.001 Å. The energy transmission coefficients of phonon wave packets, α , are also presented for reference.

B. Dislocation segments

The Granato-Lücke model^{16,21} predicts the existence of resonant modes of dislocation segments and states that the resonant frequency of a dislocation segment is inversely proportional to its length. However, to date, there has been no clear-cut demonstration or examination conducted regarding the prediction. In Sec. III A, we demonstrated the existence of the resonant modes of mobile dislocations and their resonant interactions with STA phonons at certain resonant frequencies. In this section, we will investigate the resonant modes of dislocation segments and their relationship with dislocation lengths. Figure 9 presents the mode-specific energy transmission coefficients of STA phonon wave packets across the dislocation segments with lengths ranging from 5 to 20 nm. The results of the mobile dislocation are presented in Fig. 9 as well. It should be noted that infinite-length mobile dislocations do not exist in real materials; rather, they serve as an ideal case in this work to enhance our understanding of dynamic phonon-dislocation interaction.

Figure 9 shows that the phonon transmission coefficients across each of the dislocation segments exhibit multiple minima at specific frequencies, indicating the presence of resonant modes in these segments, similar to those in the infinite-length mobile dislocation. In Fig. 10, we present a visualization of the first four resonant modes of the 10 nm-long dislocation segment (from low to high resonant frequency) through a series of time-sequence snapshots depicting the displacements of the atoms near the dislocation segment. From Fig. 10(a), it is evident that the dislocation segment undergoes large-amplitude out-of-phase vibrations at resonance, similar to the mobile dislocation. Moreover, the low-order resonant modes of the dislocation segment exhibit a shape resembling a halfsine wave, while the high-order resonant modes exhibit a shape consisting of more sine waves. This finding also applies to other dislocation segments with different lengths.

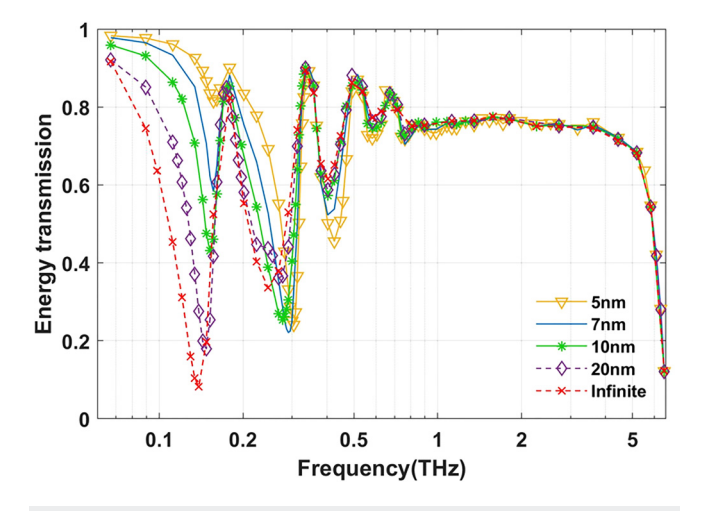


FIG. 9. The mode-specific energy transmission coefficients of STA phonon wave packets across the dislocation segments with varying lengths and the mobile dislocation with infinite length.

According to the Granato-Lücke model, 16,21 the dislocation strain in the (n + 1)th resonant mode exhibits a shape composed of (2n + 1)/2 sine waves (n = 0,1,2,3, ...). As shown in Fig. 10 (first column), the dislocation displacement for the first resonant mode aligns with a half-sine wave, which is in good agreement with the model's prediction. However, for the other resonant modes, the number of sine waves in the dislocation displacements with respect to the mode order is lower than what the model predicts. For example, in the case of the 4th resonant mode depicted in Fig. 10 (4th column), the dislocation displacement takes on a shape comprising 1.5 sine waves, whereas the Granato-Lücke model predicts 3.5 sine waves.

In Table I, we list the resonant frequencies of the first four modes for dislocation segments with lengths ranging from 5 nm to 20 nm, as well as the resonant frequencies of the infinite-length mobile dislocation. Additionally, the energy transmission coefficients of STA phonons across the dislocations at the resonant frequencies are also presented in Table I. The findings from Table I are summarized as follows.

- (1) The resonant frequencies of dislocations with different lengths, including the infinite-length mobile dislocation, are found to be close. The longer dislocation segment exhibits relatively lower resonant frequencies, but the difference is small.
- (2) The distribution of the resonant frequencies of each dislocation segment exhibits a degree of linearity. For example, the resonant frequencies of the 5 nm-long dislocation segments are 0.157 THz, 0.304 THz, 0.425 THz, and 0.582 THz, which is a nearly linear distribution.
- (3) The order of the mode corresponding to the strongest phonon scattering and lowest phonon energy transmission coefficient 8 (i.e., dominant resonant mode) varies with the length of the dislocation. For the infinite length and 20-nm-long dislocations, the dominant resonant mode is the first resonant mode. For the 10, 7, and 5-nm-long dislocations, the dominant resonant mode is the second resonant mode. The dominant resonant frequency for each dislocation is indicated by an asterisk in Table I.

The Granato-Lücke model^{16,21} predicts that the resonant frequency of the (n + 1)th resonant mode of the dislocation segment with a length of L is proportional to (2n + 1)/L. This prediction has two notable features: first, the resonant frequencies exhibit a linear distribution with respect to the mode order; and second, the resonant frequencies are inversely proportional to the dislocation length. Our simulation results confirm the model's prediction regarding the linear distribution of the resonant frequencies. However, the model's prediction regarding the inversely proportional relationship between resonant frequencies and dislocation lengths is examined to be incorrect. The Granato-Lücke model¹⁰ also predicts that the first resonant mode of dislocation leads to the strongest scattering of phonons and is the dominant resonant mode. However, the simulation results show that the dominant resonant mode does not always align with the first resonant mode of the dislocation. It can be the second resonant mode, depending on the dislocation length.

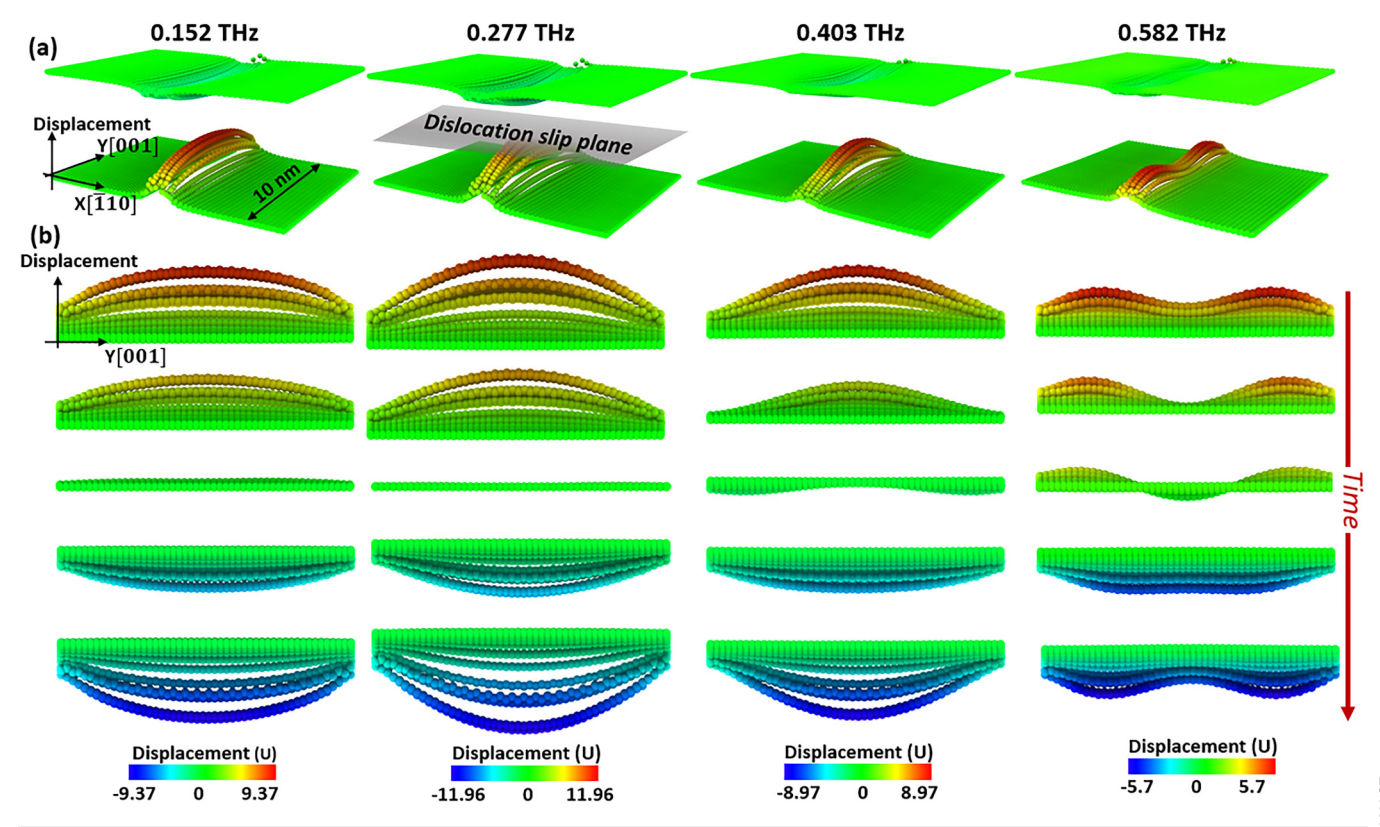


FIG. 10. (a) Perspective-view snapshots of the displacements of the atoms within the two layers at the slip plane of the 10-nm-long dislocation segment under the STA phonons at the resonant frequencies. (b) Time-sequence side-view snapshots of the bottom layer in (a), showing the shape of the dislocation motion.

C. Effect of relative positions of dislocations on the dynamic phonon-dislocation interaction

We have illustrated the relationship between dislocation resonant frequencies and dislocation lengths. However, dislocations do

TABLE I. The resonant frequencies of the first four resonant modes of the dislocations and corresponding energy transmission coefficients of the STA phonons across the dislocations. The dominant resonant frequency for each dislocation is highlighted by an asterisk.

Dislocation length (nm)	Resonant frequencies and Energy transmission coefficients of the first four resonant modes			
5	0.157THz,	0.304THz*,	0.425THz,	0.582THz,
	81.5%	24.1%	45.5%	72.0%
7	0.157THz,	0.291THz*,	0.403THz,	0.582THz,
10	58.3%	22.1%	52.3%	73.9%
	0.152THz,	0.277THz*,	0.403THz,	0.582THz,
20	43.1%	25.4%	57.3%	74.6%
	0.148THz*,	0.269THz,	0.403THz,	0.582THz,
	17.9%	36.1%	58.7%	76.2%
Infinite	0.139THz*,	0.246THz,	0.403THz,	0.582THz,
	8.2%	33.6%	61.6%	77.2%

not always exist as individual dislocations. In this section, we investigate two specific dislocation structures: a dislocation dipole [Fig. 3(d)] and a pair of closely spaced dislocations within the same slip plane [Fig. 3(e)]. Both types of structures are commonly observed in experiments. 20,49 It is noted that both dislocation structures consist of two 10 nm-long dislocation segments, but with different relative positions. Figure 11 presents the energy transmission coefficients of STA phonons across the two dislocation structures and an individual 10 nm-long dislocation segment. Similar to an individual dislocation, the two dislocation structures exhibit multiple phonon transmission minima at specific resonant frequencies. However, their resonant frequencies are distinct from those of an individual dislocation. The dominant resonant frequencies of an individual dislocation, a dislocation dipole, and a pair of closely spaced dislocations within the same slip plane are 0.277, 0.157, and 0.295 THz, respectively. It indicates that both dislocation structures have their own resonant modes and resonant frequencies. Despite both structures consisting of 10 nm-long dislocation segments, their resonant modes and frequencies have changed from those of an individual 10 nm-long dislocation segment as a result of the interaction between neighboring dislocations.

Kneezel and Granato¹⁰ predicted that "long-wavelength phonons ($\lambda \gg d$) will excite dipoles into the optical mode of vibration (i.e., the dislocations move in opposite directions)." Here, λ

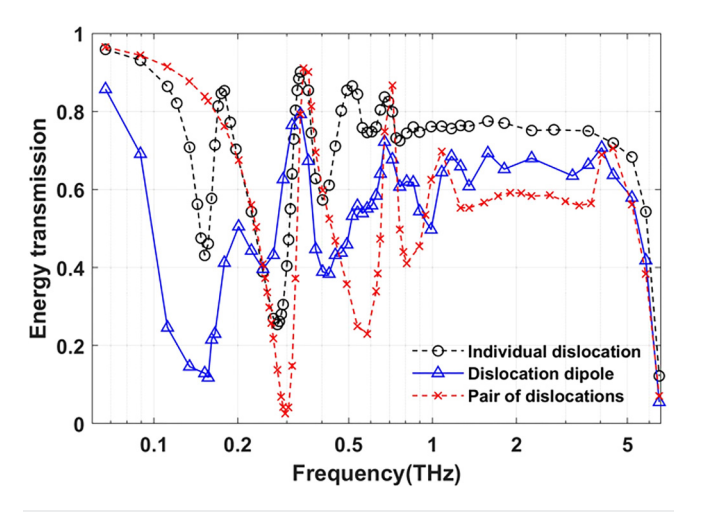


FIG. 11. The mode-specific energy transmission coefficients of STA phonon wave packets across three dislocation structures: an individual 10 nm-long dislocation segment, a dislocation dipole consisting of two 10 nm-long dislocation segments of opposite signs on closely spaced slip planes, and a pair of closely spaced 10 nm-long dislocation segments of the same sign within the same slip

denotes the phonon wavelength; d denotes the dipole spacing. In this study, we have investigated phonons with wavelengths up to 29.4 nm, which is 10 times larger than the spacing of the dislocation dipole (2.8 nm). However, no optical vibrational mode of the dislocation dipole is observed. As shown in Fig. 11, the longest wavelength phonon capable of exciting the resonance of the dislocation dipole in this study exhibits a frequency of 0.157 THz and a wavelength of 16.3 nm. The corresponding motion of the dislocation dipole during resonance is shown in Fig. 12. Similar to individual dislocations, each dislocation in the dipole exhibits largeamplitude out-of-phase vibrations. However, the two dislocations vibrate in the same phase. The only difference is that the dislocation which first encounters the phonon wave packets (dislocation 1 in Fig. 12) has a larger vibration amplitude compared to the other dislocation (dislocation 2 in Fig. 12), as the phonon wave packets are weakened after passing through the first dislocation. This result suggests that there is no optical vibrational mode of the dislocation dipole. It is also observed that the two closely spaced dislocations within the same slip plane vibrate in the same phase during resonance, while each dislocation exhibits out-of-phase vibrations. No optical vibrational mode has been observed in this scenario either.

IV. SUMMARY AND DISCUSSION

We have conducted phonon wave packet simulations to investigate the dynamic interactions between phonons and dislocations in LiF. We have quantified the mode-specific phonon transmission coefficients across five dislocation structures and studied the dislocation motions during interactions with phonon wave packets. The major findings are summarized as follows.

- 1. By comparing the phonon scattering by mobile and that by pinned dislocations, we have demonstrated that there are strong dynamic interactions between low-frequency STA phonons and mobile dislocations in LiF. This leads to the significantly stronger thermal resistance of mobile dislocations compared to pinned dislocations at low temperatures. This result is in good agreement with the experimental observations 3,10 agreement with the experimental observations.^{3,10}
- 2. The simulations have demonstrated that the dynamic interactions are essentially the excitation of resonant vibrational modes of disare essentially the excitation of resonant vibrational modes of dislocations by STA phonons, with each dislocation exhibiting a 23 series of modes that resonate with phonons of corresponding

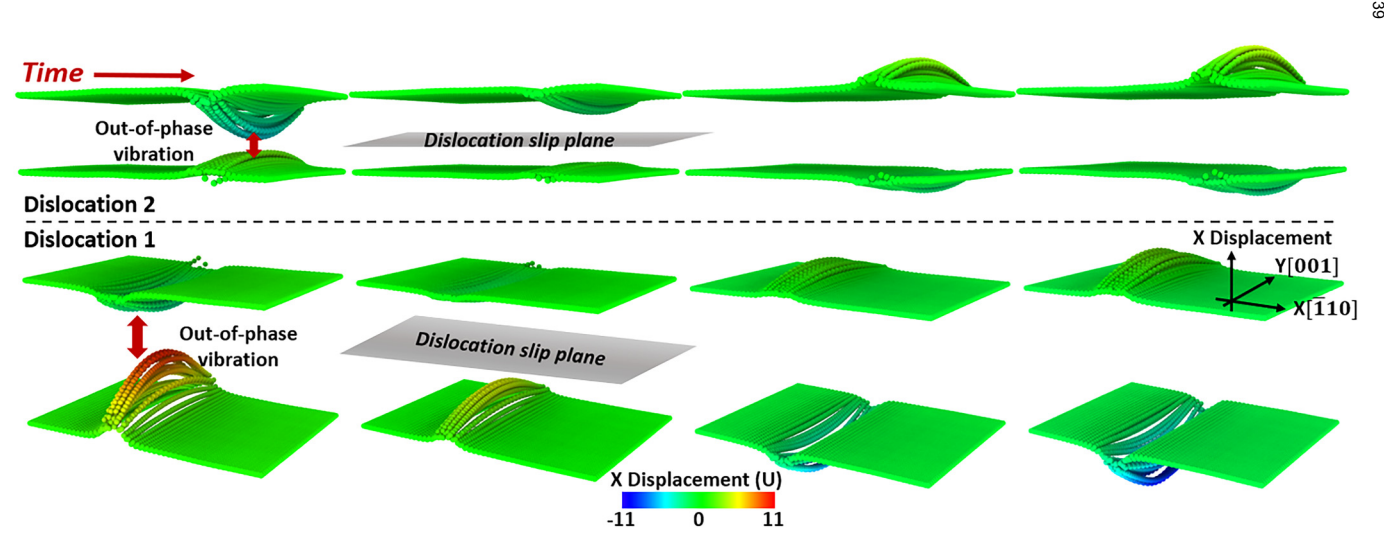


FIG. 12. Time-sequence snapshots of the displacements of the atoms within the four layers at the slip planes of the two dislocations in the dislocation dipole under the STA phonon with frequency of 0.157 THz and wavelength of 16.3 nm. Dislocations 1 and 2 refer to the order in which the dislocations in the dipole encounter the phonon wave packets in the simulations.

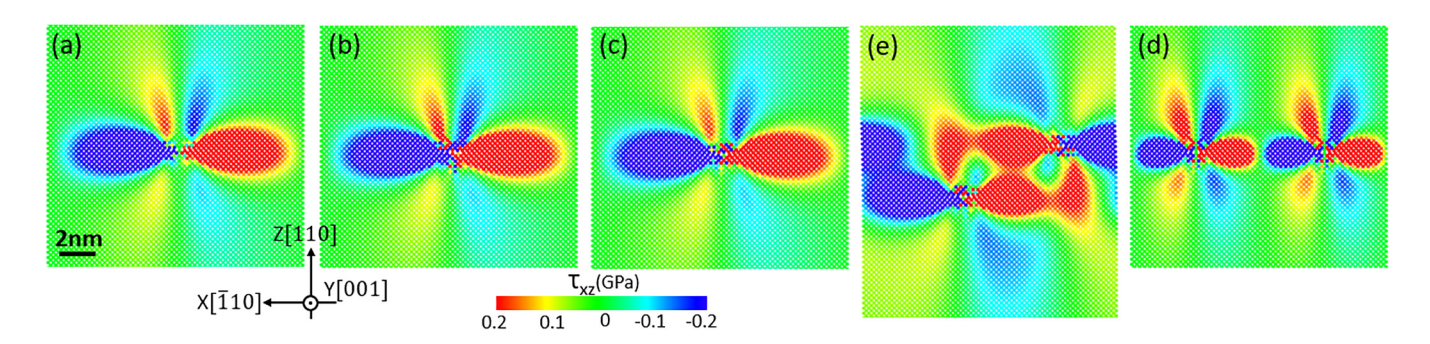


FIG. 13. Distribution of stress τ_{xy} near the dislocation core of five types of dislocations: (a) a mobile dislocation, (b) a pinned dislocation, (c) a dislocation segment, (d) a dislocation dipole consisting of two dislocation segments of opposite signs on closely spaced slip planes, and (e) a pair of closely spaced dislocation segments of the same sign within the same slip plane. The stress is calculated using the atomic virial stress formula, which is an approximation of the mechanical stress.

frequencies. During resonance, a dislocation segment undergoes significant out-of-phase vibrations with sine-wave shapes.

- 3. By investigating dislocation segments with various lengths, we found that the resonant frequencies of a dislocation exhibit a weak correlation with its length. For example, the first four resonant frequencies of a 20 nm-long dislocation segment are 0.148, 0.269, 0.403, and 0.582 THz, which are close to those of a 5 nm-long dislocation segment: 0.157, 0.304, 0.425, and 0.582 THz.
- 4. The simulation results have revealed that each dislocation possesses a dominant resonant mode, which does not always correspond to the first resonant mode of the dislocation as predicted by the vibrating string model. 16,21 Instead, the dominant resonant mode depends on the length of the dislocation. Specifically, for the dislocations investigated in this study with longer dislocation lengths (i.e., 10, 20 nm, and infinite length), their dominant resonant mode aligns with the first resonant mode of the dislocation. In contrast, for dislocations with shorter lengths (i.e., 5 and 7 nm), their dominant resonant mode corresponds to the second resonant mode of the
- 5. By investigating the dislocation dipole and a pair of closely spaced dislocations of the same sign within the same slip plane, we have demonstrated the influence of the interactions between neighboring dislocations on their resonant modes.

This study has also examined certain predictions by the vibrating string model^{16,21} that were widely discussed but not yet adequately tested. The vibrating string model's prediction of an inversely proportional relationship between dislocation length and dislocation resonant frequencies has been shown to be incorrect, as only a weak correlation between the dislocation resonant frequencies and dislocation lengths is found in this study. The vibrating string model's prediction of dislocation strain taking the shape of a sine wave at resonance was consistent with our simulation result. However, the model's predictions regarding the period of the sine wave shape of the dislocation strain in terms of dislocation length, as well as the assumption that the first resonant mode of the dislocation always leads to the strongest phonon scattering, have been shown to be not true. In addition, our investigation has refuted the

existence of optical vibrational modes of dislocation dipoles, which was a prediction put forth by Kneezel and Granato.¹

In this study, we observed a strong dynamic interaction between phonons and dislocations in LiF. Our previous research also noted strong dynamic interactions between phonons and misfit dislocations in PbTe/PbSe heterostructures.⁵⁰ Experimental studies have demonstrated that in NaCl-type structures, such as LiF, NaF, NaCl, and KCl, 5,6 strong dynamic phonon-dislocation interactions exist. It is worth noting that both PbTe and PbSe are NaCl-type structures. This supports the notion that materials with NaCl-type structures have a dynamic phonon-dislocation interaction mechanism. Future research might expand to encompass more materials with NaCl-type structures and those with different crystal. materials with NaCl-type structures and those with different crystal structures to develop a general understanding of which material platforms exhibit this dynamic interaction mechanism.

We would also like to note certain limitations that open $\frac{\omega}{\omega}$ avenues for future research. Although we have investigated different polarization vectors, we specifically focused on the phonons that have wavevectors perpendicular to the slip planes of dislocations. In Sec. II B, we have explained that the reason for choosing this group of phonons is that we can compare our simulation results with experimental measurements^{3,10} (see Fig. 2). The string model predicts that the strongest dynamic phonon-dislocation interaction occurs when the phonon stress lies across the glide plane and along the Burgers vector of the dislocation. Our simulation results show that this applies to the interaction between STA phonons and dislocations. However, phonon-dislocation interactions are complex, involving phonons from throughout the Brillouin zone and interactions with dislocations at various angles. The dependence of the dynamic interaction on the incident angle of the phonon to the dislocation still requires further investigation.

The largest investigated dislocation length in this work is 20 nm, which is limited by the length scale constraint of MD. It is unclear whether the dynamic response of dislocations with micrometer-scale lengths to phonon excitations differs from that of dislocations with nanometer-scale lengths. In addition, the investigated dislocation structures in this study are still relatively simple, while dislocation structures can be very complex in real materials. 51,52 It remains to be explored whether the dynamic phonondislocation interaction exhibits additional features when the dislocation structure is a complex dislocation network. Addressing these issues may require concurrent multiscale simulations, such as the Concurrent Atomistic-Continuum (CAC) method, ^{53,54} in future research. We have taken a step forward in this direction in our study of resonant interaction between phonons and PbTe/PbSe (001) misfit dislocation networks, which demonstrated the presence of collective motions of dislocations and phonons. ⁵⁰

ACKNOWLEDGMENTS

This work is based on research supported by the U.S. National Science Foundation under Award No. CMMI-2054607. The work of Y.L. is also partially supported by Grant No. DMR 2121895. The computer simulations are funded by the Advanced Cyberinfrastructure Coordination Ecosystem: Services & Support (ACCESS) allocation No. TG-DMR190008.

AUTHOR DECLARATIONS

Conflict of Interest

The authors have no conflicts to disclose.

Author Contributions

Yang Li: Data curation (lead); Formal analysis (lead); Investigation (lead); Methodology (lead); Visualization (lead); Writing – original draft (lead). Zexi Zheng: Formal analysis (supporting); Methodology (supporting); Writing – review & editing (equal). Xiang Chen: Methodology (equal); Writing – review & editing (equal). Youping Chen: Funding acquisition (lead); Project administration (lead); Resources (lead); Supervision (lead); Writing – original draft (supporting); Writing – review & editing (equal).

DATA AVAILABILITY

The data that support the findings of this study are available from the corresponding author upon reasonable request.

APPENDIX: LOCAL STRESS NEAR THE DISLOCATION CORE

Distribution of stress τ_{xy} near the dislocation core of five types of dislocations (Fig. 13).

REFERENCES

- ¹P. G. Klemens, Proc. Phys. Soc. A 68, 1113 (1955).
- ²P. Carruthers, Rev. Mod. Phys. 33, 92 (1961).
- ³E. P. Roth and A. C. Anderson, Phys. Rev. B 20, 768 (1979).
- ⁴Y. Kogure and Y. Hiki, Journal of the Physical Society of Japan 38, 471 (1975).
- ⁵R. L. Sproull, M. Moss, and H. Weinstock, J. Appl. Phys. 30, 334 (1959).
- ⁶T. Suzuki and H. Suzuki, J. Phys. Soc. Jpn. **32**, 164 (1972).
- ⁷M. Moss, J. Appl. Phys. 37, 4168 (1966).
- ⁸A. Taylor, H. R. Albers, and R. O. Pohl, J. Appl. Phys. 36, 2270 (1965).
- ⁹G. A. Northrop, E. J. Cotts, A. C. Anderson, and J. P. Wolfe, Phys. Rev. B 27, 6395 (1983).
- ¹⁰A. C. Anderson and M. E. Malinowski, Phys. Rev. B 5, 3199 (1972).
- ¹¹E. J. Cotts, D. M. Miliotis, and A. C. Anderson, Phys. Rev. B **24**, 7336 (1981).
- ¹²I.-S. Yang, A. C. Anderson, Y. S. Kim, and E. J. Cotts, Phys. Rev. B 40, 1297 (1989).

- ¹³J. D. Eshelby, Proc. R. Soc. Lond. Ser. A **197**, 396 (1949).
- ¹⁴F. R. N. Nabarro, Proc. R. Soc. Lond. Ser. A **209**, 278 (1951).
- ¹⁵J. S. Koehler, Imperfections in Nearly Perfect Crystals (John Wiley and Sons, Inc., New York, 1952), Vol. 197, p. 197.
- ¹⁶A. v. Granato and K. Lücke, J. Appl. Phys. 27, 583 (1956).
- ¹⁷A. Granato, Phys. Rev. 111, 740 (1958).
- ¹⁸T. Ninomiya, J. Phys. Soc. Jpn. **25**, 830 (1968).
- ¹⁹J. A. Garber and A. V. Granato, J. Phys. Chem. Solids **31**, 1863 (1970).
- ²⁰G. A. Kneeze and A. V. Granato, Phys. Rev. B 25, 2851 (1982).
- ²¹ A. V. Granato and K. Lücke, J. Appl. Phys. 27, 789 (1956).
- ²²A. Maurel, J.-F. Mercier, and F. Lund, J. Acoust. Soc. Am. 115, 2773 (2004).
- ²³ M. Li, Z. Ding, Q. Meng, J. Zhou, Y. Zhu, H. Liu, M. S. Dresselhaus, and G. Chen, Nano Lett. 17, 1587 (2017).
- ²⁴M. Li, J. Phys.: Condens. Matter **31**, 083001 (2019).
- ²⁵P. K. Schelling, S. R. Phillpot, and P. Keblinski, *Phys. Rev. B* **65**, 144306 (2002).
- ²⁶B. Deng, A. Chernatynskiy, P. Shukla, S. B. Sinnott, and S. R. Phillpot, J. Nucl. Mater. 434, 203 (2013).
- ²⁷Y. Sun, Y. Zhou, J. Han, M. Hu, B. Xu, and W. Liu, J. Appl. Phys. **127**, 045106 (2020)
- ²⁸Y. Sun, Y. Zhou, J. Han, W. Liu, C. Nan, Y. Lin, M. Hu, and B. Xu, Npj Comput. Mater. 5, 1 (2019).
- 29 J. Sun, Y. Li, Y. Karaaslan, C. Sevik, and Y. Chen, J. Appl. Phys. 130, 035301 (2021).
- 30Y. Ni, S. Xiong, S. Volz, and T. Dumitrică, Phys. Rev. Lett. 113, 124301 (2014).
- ³¹T. Wang, J. s. Carrete, N. Mingo, and G. K. H. Madsen, ACS Appl. Mater. Interfaces 11, 8175 (2019).
- 32 L. Lindsay, R. Hanus, and C. A. Polanco, JOM 74, 547 (2022).
- ³³P. K. Schelling, S. R. Phillpot, and P. Keblinski, Appl. Phys. Lett. 80, 2484 (2002).
- 34D. A. Young, Nucl. Instrum Methods Phys. Res. B 225, 231 (2004).
- 35Y. Ishii, K. Sato, M. Salanne, P. A. Madden, and N. Ohtori, J. Phys. Chem. B 118, 3385 (2014).
- ³⁶A. B. Belonoshko, R. Ahuja, and B. Johansson, *Phys. Rev. B* **61**, 11928 (2000).
- ³⁷J. D. Gale and A. L. Rohl, Mol. Simul. **29**, 291 (2003).
- ³⁸G. Dolling, H. G. Smith, R. M. Nicklow, P. R. Vijayaraghavan, and M. K. Wilkinson, Phys. Rev. **168**, 970 (1968).
- 39 R. E. Jones and D. K. Ward, Phys. Rev. B 94, 014309 (2016).
- 40 R. E. Jones and D. K. Ward, Phys. Rev. B 97, 054103 (2018).
- ⁴¹J. S. Nadeau, J. Appl. Phys. **33**, 3480 (1962).
- 42R. Landauer, IBM J. Res. Dev. 1, 223 (1957).
- ⁴³J. S. Wang, J. Wang, and J. T. Lü, Eur. Phys. J. B **62**, 381 (2008).
- 44 E. S. Landry and A. J. H. McGaughey, Phys. Rev. B 80, 165304 (2009).
- 45T. Tadano, Y. Gohda, and S. Tsuneyuki, J. Phys.: Condens. Matter 26, 225402 (2014).
- (2014).
 ⁴⁶Z. Zheng, X. Chen, B. Deng, A. Chernatynskiy, S. Yang, L. Xiong, and Y. Chen, J. Appl. Phys. 116, 073706 (2014).
- ⁴⁷G. A. Alers and J. R. Neighbours, Rev. Mod. Phys. **31**, 675 (1959).
- ⁴⁸E. J. Cotts, S. E. Shore, and A. C. Anderson, J. Phys. Chem. Solids **44**, 865 (1983).
- 49W. G. Johnston and J. J. Gilman, J. Appl. Phys. 31, 632 (1960).
- 50 Y. Li, Z. Zheng, A. Diaz, S. R. Phillpot, D. L. McDowell, and Y. Chen, Acta Mater. 237, 118143 (2022).
- ⁵¹Y. Li, B. Gu, A. Diaz, S. R. Phillpot, D. L. McDowell, and Y. Chen, Acta Mater. 260, 119308 (2023).
- 52 Y. Li, Z. Fan, W. Li, D. L. McDowell, and Y. Chen, J. Mater. Res. 34, 2306 (2019).
- 53Y. Chen, S. Shabanov, and D. L. McDowell, J. Appl. Phys. 126, 101101 (2019).
- ⁵⁴A. Diaz, B. Gu, Y. Li, S. J. Plimpton, D. L. McDowell, and Y. Chen, J. Comput. Phys. 463, 111140 (2022).
- 55Y. Chen and A. Diaz, Phys. Rev. E 98, 052113 (2018).
- **56**Y. Chen and A. Diaz, Phys. Rev. E **94**, 053309 (2016).
- 57Y. Chen, Europhys. Lett. 116, 34003 (2016).